26th International Congress on Modelling and Simulation, Adelaide, SA, Australia, 30 Nov–4 Dec 2025
mssanz.org.au/modsim2025

Simulation of Ember Transport Around Urban Structures

Lachlan Cunningham [a]. James Hilton [b], Murray Rudman [a]

[a] *Monash University, Melbourne, VIC, Australia*
[b] *Covey Associates, Maroochydore, QLD, Australia*
Email: james.hilton@covey.com.au

Abstract:

Understanding the transport and distribution of embers from a wildfire is crucial in planning, mitigation and building design, especially at the wildland-urban interface (WUI) in high-risk regions. Embers can accumulate on combustible surfaces or penetrate gaps in structures leading to structural damage or loss far from the main fire front and independent of direct flame contact and radiant heat effects. However, quantifying ember transport is challenging both from an experimental and modelling perspective. The dynamics of embers near a wildfire are governed by turbulent flow resulting from the interaction of external wind fields and strong buoyant fire plumes. Recent studies have used computational modelling to simulate such flow fields and gain insights into the structures within fire plumes as well as the dynamics of particles transported within these fields. Such studies discovered elements within the plume such as vortex rolls that lead to distinct patterns in ember transport and distribution at different wind speeds, as well as evaluated many different fire and vegetation geometries.

The influence of obstacles or structures on the flow field has received less attention. In this study we model an idealised fire under the influence of an external wind field and investigate the effect of obstacles, representing structures approximately the size of a standard Australian house at the WUI. The model used the CFD package OpenFOAM with a static heat source representing the fire and one to twelve structures arranged to represent the layout of rows of houses. Embers were modelled as particles passively transported with the flow with diameters from 1.5 to 5 mm. The wind speed was varied from 4.5 to 10 ms^{-1}, and the flow field, particle velocity and landing distributions were recorded.

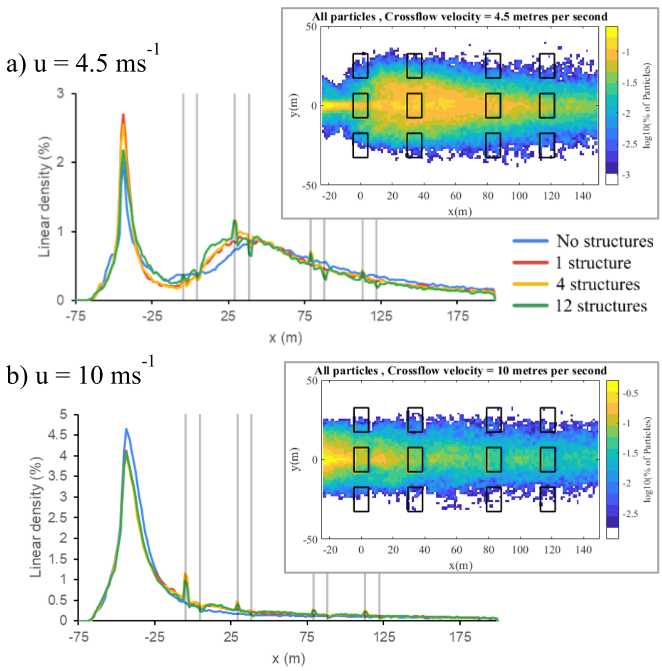

Figure 1 – Percentage ember density as a function of streamwise position (plots) and top-down view of resultant logarithmic density distribution (insets) for a) 4.5 ms^{-1} and b) 10 ms^{-1} wind speeds. Plots show 0-12 structures, insets show 12 structure case. Vertical lines show structure positions.

Our findings show strong sensitivity to wind speed for both the flow field and subsequent ember landing distributions. This is due to a transition from plume-dominated to wind-driven dynamics at higher wind speeds. The effect of this can be seen in Fig.1, most notably an increase in ember density on the second row of structures at low wind speeds (second peak at ~50 m in Fig 1a), in contrast to a distribution that may be expected by assuming a linearly decreasing ember density from the fire, as occurs at higher wind speeds (no secondary peak in Fig 1b). There was less, though significant, sensitivity to the layout of the solid structures. Observed effects included channelling of the flow between structures, with a resultant ember flux of the portions of structures parallel to the prevailing wind at ground level, and recirculation effects in the lee of structures.

Current wildfire models and standards necessarily simplify the expected pattern of ember distribution for risk exposure metrics, for example the Australian AS3959 standard. The findings here indicate that the wind speed and pattern of structures has a significant effect on ember flux and these, as well as secondary effects such as channelling and recirculation leading to ember accumulation, may need to be accounted for in such metrics.

Keywords: *Ember attack, Fire risk, Wildland-urban interface, Computational modelling*

1. INTRODUCTION

Wildfire impact on urban areas, especially at the wildland urban interface, is a major focus of current risk modelling and research effort. Wildfire effect on structures comprises three main categories: direct flame contact, radiant heat exposure and ember attack. Direct flame contact between built structures and fires are well understood due to decades of research in fire engineering and material science, and structure impact is relatively straightforward to simulate using wildfire spread modelling. Radiant heat flux is also well understood with a geometric physical basis, although modelling of radiant heat flux is extremely complex in real-world environments due to the requirement of line-of-sight calculations. However, simplified radiant heat flux models provide a reasonable approximation of radiant heat flux and are used as the basis of some fire risk and building code models (Standards Australia, 2009).

Embers are the most difficult of the three attack methods to quantify, despite being the prevalent cause of house loss in wildfires (Blanchi *et al.* 2006). There are multiple mechanisms of loss or damage from ember attack including penetration of gaps in the building envelope, accumulation of embers on combustible materials and entry to the building via broken windows or fittings (Leonard and Blanchi 2005). The difficulty of resolving ember dynamics is due to many factors including the challenge of capturing the behaviour of embers in flight during a live fire, the sensitivity to environmental conditions and the difficulty of modelling ember transport to a degree capable of informing generalised risk analysis. However, much recent progress has been made including the development of dedicated experimental facilities to produce embers and impact on structures and capturing ember paths in flight (Wickramasinghe 2022). On the modelling side much work has focused on the passive transport of embers and firebrands in flow fields generated by a range of wildfire conditions (Saurav 2023, Thurston 2017), as well as detailed modelling of individual ember transport dynamics based on experimentally measured characteristics (Koo 2010, Wickramasinghe 2022, Alonso-Pinar 2025). Saurav *et al.* (2023) carried out a detailed study of ember transport around structures at a wildland-urban interface, showing the mechanism behind streaming plumes of ground-level embers, similar to those also observed in this study.

In this study we investigate the effect of wind speed and structural configuration on ember distribution using the OpenFOAM computational fluid dynamics (CFD) package. As with all such models only a simplified approximation of the endlessly complex variation of wildfire conditions and urban configurations can be simulated. However, we show the strong sensitivity to wind conditions on the resulting ember distribution with significant implications for future risk considerations from ember attack. As a note for clarity, we only consider embers in this study, defined here as small burning fuel elements less than 5 mm in effective diameter within around 100 m from the fire, rather than firebrands which are larger burning fuel particles that travel longer distances. The definitions of these terms are sometimes mixed in the literature, but here we are only considering short-range effect near urban structures, rather than long-range firebrands that can lead to fire spotting or other secondary effects.

2. METHODS

The simulations consisted of a three-dimensional rectangular domain with dimensions of 1.5×0.8×0.4 km in the streamwise, spanwise and vertical directions containing a circular heat source, used to represent a wildfire, and an array of 3 metres tall rectangular solid objects, representing structures in an urban area as shown in Fig. 2. The size and spacing of these were taken as the approximate size and shape of an Australian dwelling, with the width of a road gap between the second and third columns. To investigate the influence of these structures, a single structure, a single row (four structures) and three rows (twelve structures) were used in the simulations.

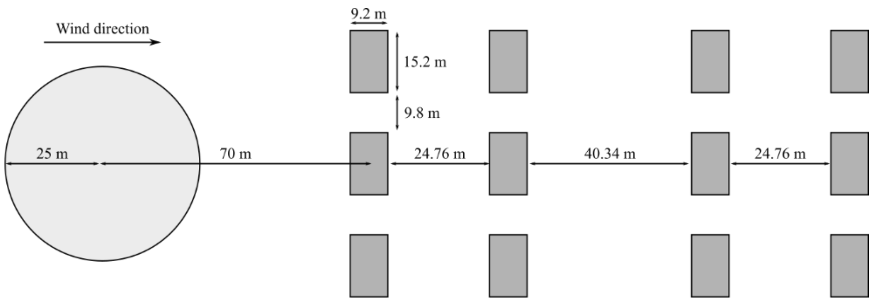

Figure 2 Simulation set up with three rows of structures, coloured dark grey. Fire area shown as light grey circle on left hand side.

As the focus of this study is fire-induced flow and subsequent particle transport, combustion modelling was not undertaken and the fire was approximated by a constant and spatially fixed volumetric heat source with diameter of 50 m, height 3 m and a heat release rate set to 1000 MW, giving a heat flux of 509.3 kW m^{-2} with a Rothermel flame height equivalent of 6 m. Because the wind speed is substantially higher than the rate of spread of the fire, this simplification was not expected to significantly alter the trajectory of firebrands. The wind direction was set parallel to the long axis of the domain from the heat source towards the structures.

The *reactingParcelFoam* solver from the open-source OpenFOAM library was used for the simulations. This is a transient finite volume method solver for buoyant particle-laden flows which involve heat transfer. A Large Eddy Simulation approach (Thurston 2017) was used to resolve the large-scale turbulence features of the flow. The atmosphere was treated as a single incompressible phase. Velocity and pressure coupling were managed by the 'PIMPLE' algorithm which combines the PISO and SIMPLE algorithms to solve the governing equations for continuity (Eq. 1), momentum (Eq. 2) and enthalpy (Eq. 3), where terms related to the disabled sub models have been excluded.

$$\frac{\partial \rho}{\partial t} + \nabla \cdot (\rho u) = 0 \qquad [1]$$

$$\frac{\partial (\rho u)}{\partial t} + \nabla \cdot (\rho u u) = -\nabla p + \rho g + \nabla \cdot \left(2\mu_{eff} D(u)\right) - \nabla \left(\frac{2}{3}\mu_{eff}(\nabla \cdot u)\right) \qquad [2]$$

$$\frac{\partial (\rho h)}{\partial t} + \nabla \cdot (\rho u h) + \frac{\partial (\rho K)}{\partial t} + \nabla \cdot (\rho u K) - \frac{\partial p}{\partial t} = \nabla \cdot \left(\alpha_{eff} \nabla h\right) + \rho u \cdot g \qquad [3]$$

Where μ_{eff} is the effective viscosity, defined as the sum of the eddy and molecular viscosities, ρ is density, u is the velocity vector, $D(u)$ is the rate of strain tensor and K is defined as the kinetic energy per unit mass. The effective thermal diffusivity, α_{eff}, is the sum of both the laminar and eddy thermal diffusivities:

$$\alpha_{eff} = \frac{\rho \nu_t}{Pr_t} + \frac{\mu}{Pr} \qquad [4]$$

The governing equations were discretised in time using the implicit Euler time scheme. The advection of enthalpy was discretized using van Leer's (1976) MUSCL differencing scheme, and Jasak's (1999) Gauss-Gamma scheme was utilised for the advection of momentum. A central differencing scheme was used for the advection of all other quantities. The wall adaptive large-eddy (WALE) turbulence model (Nicoud and Ducros, 1999) was used to model the vortices too small to be fully resolved by the computational mesh. This turbulence model can handle transition from laminar to turbulent flow and performs well near walls, making it particularly suitable for modelling air entrainment and macroscopic mixing processes (Yuen, 2016). The model has been utilised broadly for wall-bounded flows and has been demonstrated to perform well when benchmarked against other commonly used LES models in the case of a buoyant pool fire (Yuen 2016).

Embers were treated as uniform spherical Lagrangian particles, acted on by the force of gravity, drag and the result of pressure gradients within the flow. Collisions between embers were ignored and only one-way coupling was implemented as the particles were assumed too small and sparse to have an appreciable influence on the flow. In OpenFOAM the drag force acting on a sphere was expressed as:

$$F_D = m_p(u_c - u_p)\frac{3}{4}\frac{\mu_c C_D Re_p}{\rho_p d_p^2} \qquad [5]$$

Where u_c is the velocity of the carrier phase, u_p is the velocity of the particle, C_D is the drag coefficient, μ_c is the dynamic viscosity of the carrier phase and d_p, ρ_p and d_p Re_p are the particle's density, diameter and Reynold number respectively. The drag coefficient was calculated as a function of Reynold's number using Putnam (1961)'s model:

$$C_D = \begin{cases} \frac{24}{Re_p}\left(1 + \frac{1}{6}Re_p^{\frac{2}{3}}\right) & Re_p \leq 1000 \\ 0.424 & Re_p > 1000 \end{cases} \qquad [6]$$

The pressure gradient force was calculated using the material derivative of the carrier phase:

$$F_P = \frac{m_p}{\rho_p}\rho_c \frac{Du_c}{Dt} \quad [7]$$

The gravitational force acting on each particle was

$$F_G = m_p(1 - \frac{\rho_c}{\rho_p}) \quad [8]$$

Embers were injected from a patch on the ground directly beneath the heat source with a speed of 15 ms^{-1} vertically. This had the effect of injecting them at 5 m above ground level, as this initial momentum was rapidly depleted. Particles were injected over a 200 second interval at a rate of 1500 particles per second resulting in a total of 300,000 particles per simulation. The ember diameters were fixed at 1.5 mm, 2 mm, 2.5 mm, 3 mm, 3.5 mm, 4 mm, 4.5 mm and 5 mm with a uniform probability of each size being created.

The sides and top of the domain were free-slip boundaries sufficiently far away to avoid influencing the flow near the structures. The floor was a no-slip boundary and utilised wall functions for turbulent viscosity and turbulent thermal conductivity. A non-reflecting pressure outlet was used in conjunction with a fixed velocity profile at the inlet. The inlet velocity profile followed a log-law profile Yang (2009), with a reference wind speeds of 4.5 ms^{-1}, 8 $ms^{-1}$and 10 ms^{-1} set at a height of 10m above ground level:

$$u = \frac{u^*}{\kappa} ln\left(\frac{z - d + z_0}{z_0}\right) \quad [9]$$

where κ is the von Kármán constant, d is a ground normal displacement height, z_0 is the aerodynamic roughness length and u^* is the friction velocity, defined using these variables and a prescribed reference height/velocity pair:

$$u^* = \frac{u_{ref}\kappa}{ln\left(\frac{z_{ref} + z_0}{z_0}\right)} \quad [10]$$

The mesh contained 7.4 million hexahedral cells refined in 5 zones to well-resolve flow near the heat source and the houses without making the simulation prohibitively expensive. The cells had lengths ranging from 0.2 m at the edges of the houses, 0.4 m in the wake region of the houses and the heat source then progressively increasing in size to 5.6 m in the far field. Each configuration was run on a coarse grid until the plume had reached a quasi-steady state, after which the flow fields were interpolated onto the finer mesh (where each cell was approximately 1/3 the size) and run for a further simulated 300 seconds.

3. RESULTS

Instantaneous particle velocities are shown in Fig. 3 for a single row of structures with wind speeds of u = 4.5 ms^{-1} and u = 8 ms^{-1}. As can be seen there is a significant difference in the flow structure and ember distribution for this minor change in wind speed. The flow at u = 4.5 ms^{-1} is plume dominated, with embers lofted initially near-vertically before falling onto the second structure. The lack of ember flux on the first structure is a potentially significant finding and may lead to structures nearer the fire being less less affected than structures one row back. In contrast the flow at u = 8 ms^{-1} is wind-dominated with the ember flux almost parallel to the ground and horizontally impacting the first structure. The flow structure is also more pronounced at higher wind speed, matching observations of ember 'waves' or streams falling in downwind from the fire.

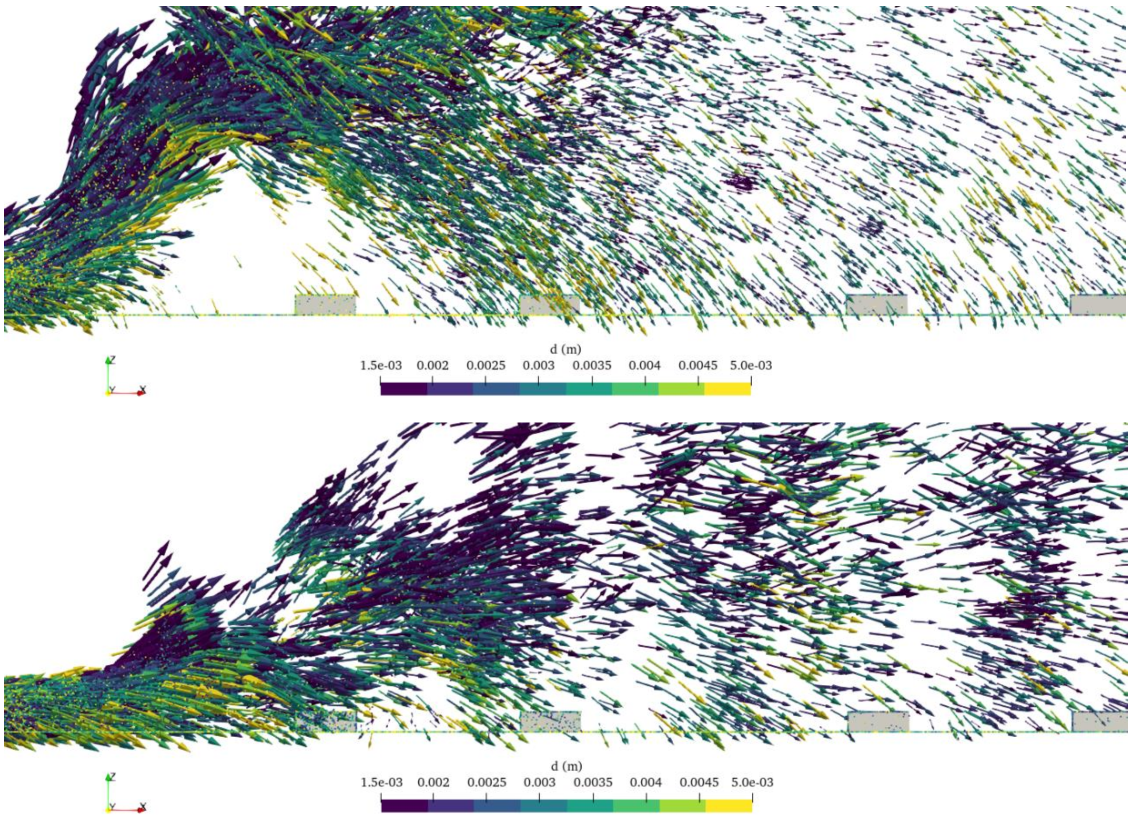

Figure 3 - Particle velocity vectors coloured by particle size for single row of structures at t = 450 s, top: u = 4.5 ms^{-1}, bottom u = 8 ms^{-1}. The structures are shown as grey blocks.

The logarithm of the overall particle density on the lower boundary is shown in Fig. 4 for wind speeds of u = 4.5 ms^{-1} and u = 8 ms^{-1}. This reflects the finding of significantly increased ember attack for the lower wind speed case on the second structure compared to the first structure nearer the fire.

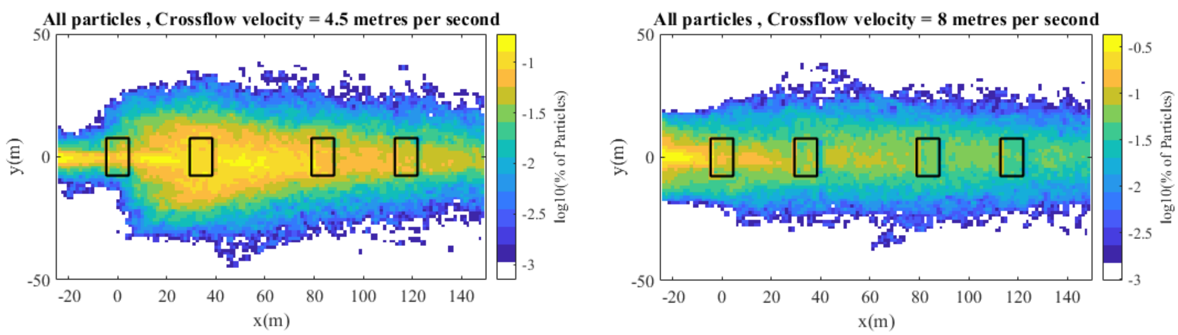

Figure 4 - Logarithm of particle number density for single row, left: u = 4.5 ms^{-1}, right u = 8 ms^{-1}. Black rectangles show positions of row of structures.

The mean wind flow fields are shown in Fig. 5 for u = 4.5 ms^{-1} and u = 8 ms^{-1} for a single row of structures. Interesting differences are apparent between these cases, notably the increased back circulation (highlighted in red) in the lee of the first structure that increases in magnitude at higher wind speeds. This will likely cause accumulation of embers behind the structure. (This effect is not modelled in the current simulations as the embers are marked where they land, future versions will include a slip condition on the lower boundary.) The second feature of note is the flow separation at higher wind speeds over the second structure (highlighted in blue). This behaviour may act to loft embers over the second structure at higher wind speeds leading to a reduction of ember flux on the roof of the structure.

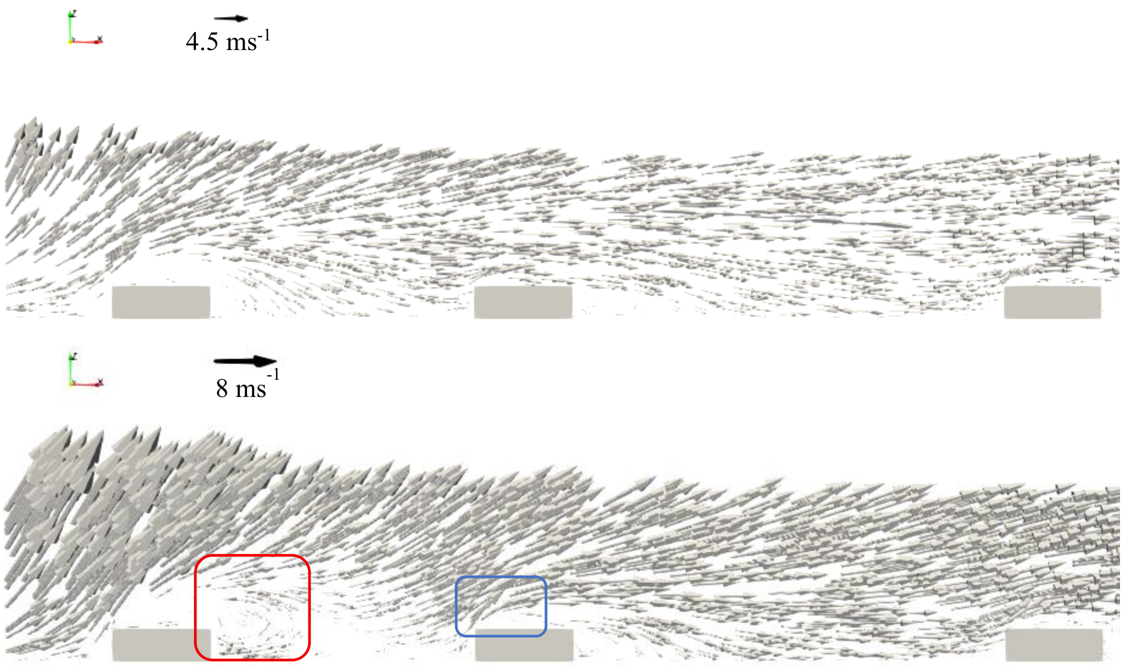

Figure 5 – Mean wind flow velocity over simulation for top: u = 4.5 ms^{-1}, bottom u = 8 ms^{-1}. Flow features are outlined, red: recirculation region in lee of first structure, blue deflection updraft leading to larger flow separation on second structure.

A top-down view of the mean velocity flow field at a height of 1.5 m above ground level for four (left column) and twelve structures (right column) is shown in Fig. 6. The vectors are coloured by speed in the vertical (z) direction, where red vectors show upward flow and blue downward flow. In all cases the fire plume causes an updraught immediately downwind of the flame zone, with lateral downflows associated with the well-known counter-rotating vortex pair structure (Forthofer, 2011). The simulations for both sets of structures show a net inward flow towards the centreline of the domain in all cases. This effect has been previously noted by Saurav *et al.* (2023) and may result in an ember flux perpendicular to the flow direction on the outer edges of the outermost structures. In all cases downstream structures are shielded at this height from the flow by upwind structures, but are subject to lateral cross flow, especially at higher wind speeds (example areas of crossflow are outlined in red in Fig. 5). This seems especially apparent in the case of twelve houses where the flow appears channelled between the first and second row of structures. Such crossflows may lead to accumulation of ground level embers at the front and sides of downstream structures, even though this flow may not be expected from the apparent wind direction and expected shielding effect of upstream structures.

4. DISCUSSION AND CONCLUSION

The distribution of embers from a fire is known to be complex and strongly affected by wind conditions and fire geometry, but are usually simplified in risk metrics based on statistical analysis or assumed linear distributions from the fire front. For example, the current method 1 Australian AS3959 building standard states 'insufficient risk' of ember risk 100 m from burning vegetation (BAL-LOW), and the next lowest risk category (BAL-12.5) simply states 'ember attack'. Many recent studies, including this, have found simplified models do not represent realistic ember distributions found in wildfire conditions. We have shown that including structures into the model further changes the distribution of the embers and the flow fields transporting these embers. Our simulations indicate that, counterintuitively, the risk from ember attack at structures further from the fire can *increase* at low winds speeds. This effect could explain reports of unexpected loss of houses downwind but one or two rows back from an active bushfire front, for example "*the majority of destroyed Tathra houses were affected by ember attack, and most of them were not even close to forest*" (Tathra Bushfires Quick Response Report, 2018) and warrants further investigation. Furthermore, three-dimensional flow effects can lead to recirculation in the lee of structures and secondary channelling perpendicular to the wind direction, causing potential ember accumulation and increased fire risk in unexpected areas. Findings such as these may need to be taken into account in the next generation of wildfire risk models and standards to improve safety and outcomes in high-risk areas.

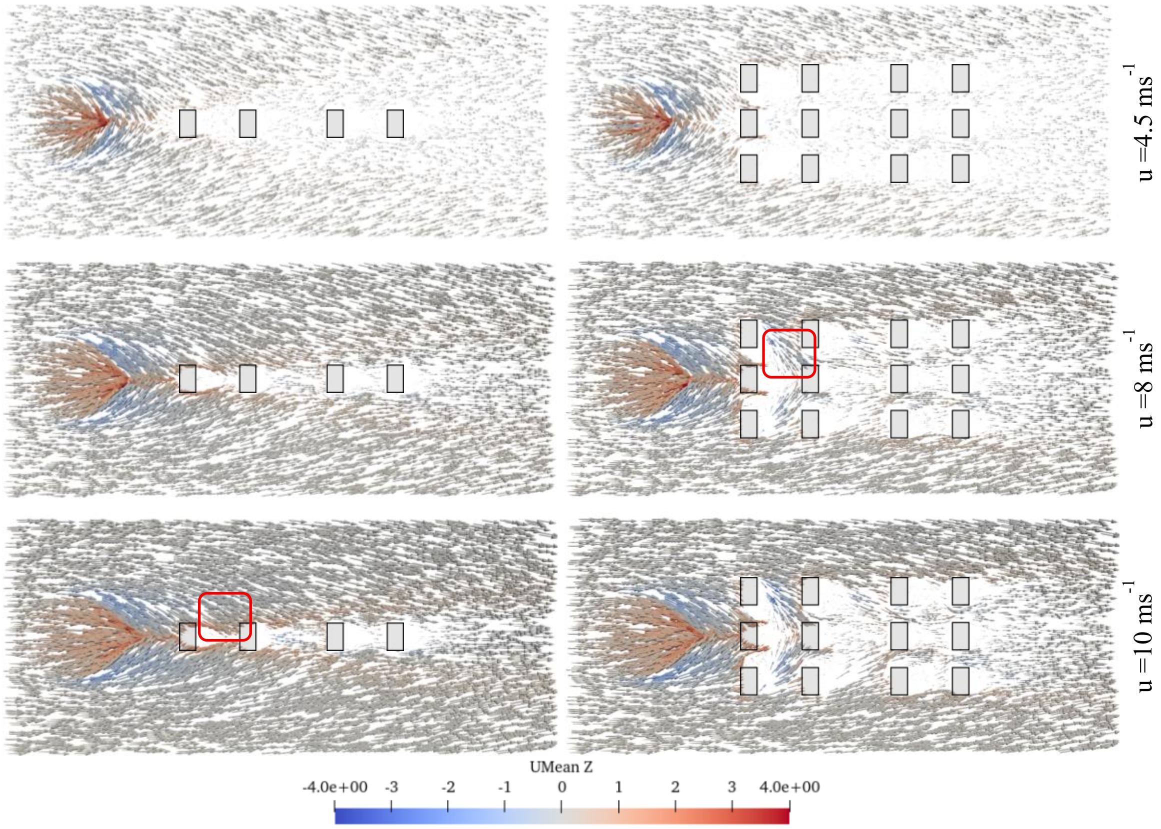

Figure 6 – Time averaged flow wind field coloured by speed in the vertical (z) direction for four and twelve structure cases and wind speeds $u = 4.5$ ms^{-1} (top), $u = 8$ ms^{-1} (middle) and $u = 10$ ms^{-1} (bottom).

REFERENCES

Alonso-Pinar A., Filippi J. B., Nguyen H. N, Filkov A. (2025) A simplified model to incorporate firebrand transport into coupled fire atmosphere models. International Journal of Wildland Fire (34), WF24200.

Blanchi, R., Leonard J., Leicester R. H. (2006). Bushfire risk at the rural/urban interface.

Forthofer, J. M., Goodrick, S. L. (2011) Review of Vortices in Wildland Fire, Journal of Combustion, 984363

Issa, R.I., 1986. Solution of the implicitly discretised fluid flow equations by operator-splitting. Journal of computational physics, 62(1), pp.40-65.

Koo, E., Pagni, P. J., Weise, D. R.; Woycheese, J. P. (2010) Firebrands and spotting ignition in large-scale fires. International Journal of Wildland Fire 19(7) 818-843

Leonard, J. and Blanchi, R. (2005) Investigation of bushfire attack mechanisms involved in house loss in the ACT Bushfire 2003. Highett, Vic., CSIRO Manufacturing & Infrastructure Technology. Bushfire CRC report

Nicoud, F., Ducros, F. (1999) Subgrid-scale stress modelling based on the square of the velocity gradient tensor. Flow, turbulence and Combustion, 62(3), 183-200.

Putnam, A. (1961) Integrable form of droplet drag coefficient. Ars Journal, 31(10), 1467-1468.

Saurav, T. M., Sutherland, D., Sharples, J. (2023) A computational framework for phenomenological modelling of ember storms at the wildland-urban interface, Proceedings of the 25th International Congress on Modelling and Simulation, 816-822

Standards Australia (2009) AS 3959, Australian Standard for construction of buildings in bushfire prone areas. Technical report, Standards Australia.

Thurston, W., Kepert, J. D., Tory, K. J., Fawcett, R. J., (2017) The contribution of turbulent plume dynamics to long-range spotting. International Journal of Wildland Fire, 26(4), 317-330.

Wickramasinghe, A., Khan, N., Moinuddin, K. (2022) Determining firebrand generation rate using physics-based modelling from experimental studies through inverse analysis. Fire, 5 (1)

Yang, Y., Gu, M., Chen, S. and Jin, X., (2009) New inflow boundary conditions for modelling the neutral equilibrium atmospheric boundary layer in computational wind engineering. Journal of Wind Engineering and Industrial Aerodynamics, 97(2), 88-95.

Yuen, A. C. Y., Yeoh, G. H., Timchenko, V., Cheung, S. C. P., Chen, T. (2016) Study of three LES subgrid-scale turbulence models for predictions of heat and mass transfer in large-scale compartment fires. Numerical Heat Transfer, Part A: Applications, 69(11), 1223-1241.

